Article

Observation of constructive interference at the edge of quantum ergodicity

https://doi.org/10.1038/s41586-025-09526-6

Received: 3 November 2024

Accepted: 13 August 2025

Published online: 22 October 2025

Open access

Check for updates

Google Quantum AI and Collaborators*

The dynamics of quantum many-body systems is characterized by quantum observables that are reconstructed from correlation functions at separate points in space and time[1–3]. In dynamics with fast entanglement generation, however, quantum observables generally become insensitive to the details of the underlying dynamics at long times due to the effects of scrambling. To circumvent this limitation and enable access to relevant dynamics in experimental systems, repeated time-reversal protocols have been successfully implemented[4]. Here we experimentally measure the second-order out-of-time-order correlators (OTOC$^{(2)}$)[5–18] on a superconducting quantum processor and find that they remain sensitive to the underlying dynamics at long timescales. Furthermore, OTOC$^{(2)}$ manifests quantum correlations in a highly entangled quantum many-body system that are inaccessible without time-reversal techniques. This is demonstrated through an experimental protocol that randomizes the phases of Pauli strings in the Heisenberg picture by inserting Pauli operators during quantum evolution. The measured values of OTOC$^{(2)}$ are substantially changed by the protocol, thereby revealing constructive interference between Pauli strings that form large loops in the configuration space. The observed interference mechanism also endows OTOC$^{(2)}$ with high degrees of classical simulation complexity. These results, combined with the capability of OTOC$^{(2)}$ in unravelling useful details of quantum dynamics, as shown through an example of Hamiltonian learning, indicate a viable path to practical quantum advantage.

Identifying complex correlations between the many-body degrees of freedom in a quantum system is a central goal for the simulation of quantum dynamics. Even spectroscopic questions can be formulated in terms of few-point dynamical correlations. As entanglement grows with system size or evolution time, the resulting dynamics are often ergodic. Consequently, the sensitivities to the details of the quantum dynamics decay exponentially for most quantum observables, limiting their utility in revealing many-body correlations. Numerical or analytical studies of correlations are also hindered by the difficulty of identifying subtle contributing processes, which undermine common simplifying assumptions. Moreover, the linearity of the Schrödinger equation precludes the use of classical techniques based on sensitivity to initial conditions, methods that have proven effective in detecting the butterfly effect and characterizing classical chaos.

As a solution to the above challenge, experimental protocols that use refocusing to echo out nearly all evolution have become essential for probing highly entangled dynamics. These protocols have proven indispensable in quantum metrology and sensing[19,20] as well as in studies of chaos, black holes and thermalization[6,8,21–23]. Dynamical sequences that include time reversal are most naturally described in the Heisenberg picture of operator evolution (Fig. 1). The sequence can be conceptualized as an interference problem, where correlations reflect coherent interference across many-body trajectories. Computing an observable can, thus, be expressed as a sum over distinct trajectories. In this conceptual framework, each time reversal corresponds to the addition of two interference arms and also other cross-terms contributing to experimental observables, which are formally known as out-of-time-order correlators (OTOCs)[5–18].

In our work, we perform a family of OTOC experiments and leverage the interference framework to understand how different paths and their combinations reveal quantum correlations inaccessible without time reversal or with numerical methods. More specifically, we use the unique programmability of a digital quantum processor to change the number of interference arms (Fig. 2) and insert either noisy (Fig. 3) or coherent (Fig. 5) phase shifters into each arm. In response, we find that OTOCs are more sensitive to these perturbations compared with observables in the absence of time reversal. Furthermore, we discover that this sensitivity is enhanced as the order k of OTOC$^{(k)}$ (the number of interference arms) increases. In particular, OTOC$^{(2)}$ reveals constructive interference between Pauli strings that is invisible in lower-order observables.

To understand how repeated time-reversal restores the sensitivity to quantum dynamics, we first consider measuring the Pauli operator $M \in \{X, Y, Z\}$ of a qubit q_m in a square lattice of qubits and initialized in an eigenstate of M. The measurement at a time t is equivalent to the time-ordered correlator (TOC), $\langle M(t)M\rangle$, where $M(t) = U^{\dagger}(t)MU(t)$ denotes the time-evolved M in the Heisenberg picture, U is a many-body unitary, and $\langle \ldots \rangle$ denotes the expectation value over a particular initial state. As observed in previous experiments[24–27], $\langle M(t)M\rangle$ decays exponentially over time when U is ergodic. This stems from the scrambling of

*A list of authors and their affiliations appears at the end of the paper.

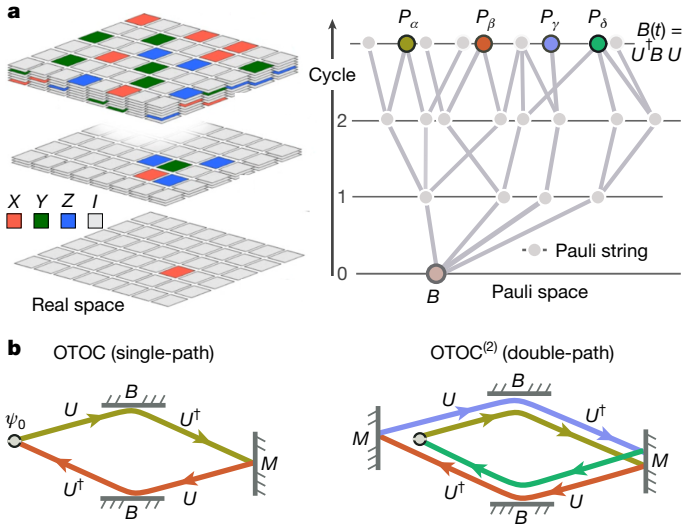

Fig. 1 | OTOCs as interferometers. a, When dynamical protocols involve echoing, the Heisenberg picture of the operator evolution is the natural framework for studying dynamics. **b**, OTOC and OTOC$^{(2)}$ can be viewed as time interferometers, which highlights their capability of refocusing on desired details and echoing out unwanted dynamics. See text for the definition of parameters.

quantum information from the initial state of q_m into the exponentially large Hilbert space of the system.

The above decay can, however, be partially refocused through the evolution outlined in Fig. 2a. Here, the dynamics U is replaced with the nested echo sequence $U_k(t) = B(t)[MB(t)]^{k-1}$, where $B(t) = U^\dagger(t)BU(t)$ is the time-evolved operator of another Pauli B acting on qubit(s) q_b some distance away from q_m and $k \geq 1$ is an integer. The action of U_k may be understood as dispersing the information injected by M, modifying it by B, reversing it back to M and repeating this process $k-1$ times. As $U_k^\dagger(t) = U_k(t)$, the expectation value (denoted as $\mathcal{C}^{(2k)}$ in this case) may be written as:

$$\mathcal{C}^{(2k)} = \langle U_k^\dagger(t) M U_k(t) M \rangle = \langle (B(t)M)^{2k} \rangle. \quad (1)$$

The quantity $\mathcal{C}^{(2)}$ coincides with the well-known out-of-time-order correlator[5–18,28], OTOC. We, therefore, refer to $\mathcal{C}^{(2k)}$ as OTOC$^{(k)}$ or kth-order OTOC. Equation (1) yields two key insights. First, if the information originating from q_m has not yet reached q_b, $B(t)$ commutes with M and the information coming back to q_m is identical to its initial value. We, therefore, expect the existence of a wavefront across which $\mathcal{C}^{(2k)}$ decays. By increasing the separation between q_m and q_b, this front may be pushed later in time, thus allowing large signals to be measured where TOCs are approximately 0. Second, provided U is not a Clifford sequence, information starting from M and returning to M can take several different paths in configuration space. Correlations between Pauli strings within $B(t)$ may, therefore, manifest through constructive interference between different paths for $\mathcal{C}^{(2k)}$ with $k \geq 2$.

Sensitivity of OTOCs to quantum dynamics

We begin by characterizing the sensitivity of OTOC$^{(2)}$ to the microscopic details of quantum dynamics. Figure 2a schematically shows our quantum circuits, which are composed of random single-qubit and fixed two-qubit gates. The experiment is done by first fixing the choices of q_m and q_b. A circuit instance i is then generated by varying the random parameters of the single-qubit gates that interleave the deterministic set of two-qubit gates. For a fixed number of circuit cycles t within U, the quantity $\mathcal{C}^{(2k)}(t, q_m, q_b, i)$ is repeatedly measured until the statistical noise of the measurement is less than 10% of its average value. This protocol is then repeated by varying t, q_m and q_b, as well as the circuit instance i, which is sampled 50 to 250 times. Last, all experimental $\mathcal{C}^{(4)}$ or $\mathcal{C}^{(2)}$ values are normalized by a global rescaling factor obtained through error-mitigation strategies (Supplementary Information sections II.E.1 and II.F.1).

The top row of Fig. 2b displays the values of $\overline{\mathcal{C}}^{(4)}(t, q_b)$ for different circuit cycles and choices of q_b, where the overline denotes averaging over circuit instances. The location of q_m is fixed throughout these measurements. The information front introduced above is clearly visible in the experimental data. For each t, there is a boundary for q_b beyond which $\mathcal{C}^{(4)}$ is approximately 1. This boundary defines the light cone of q_m, which corresponds to the set of qubits that have been entangled with q_m. Moreover, we find that the circuit-to-circuit fluctuation of $\mathcal{C}^{(4)}(t, q_b)$, defined as the standard deviation σ of its value over circuit instances, is of the same order of magnitude as the average value near the information front (bottom row of Fig. 2b). This observation indicates that $\mathcal{C}^{(4)}$ is, indeed, highly sensitive to the details of the underlying evolution U, an effect that we will later use to demonstrate its application in Hamiltonian learning.

To study more systematically the decay of OTOC sensitivity over time, we measure the standard deviations of various OTOCs as functions of t (Fig. 2c). We observe that the standard deviations of $\mathcal{C}^{(2)}$, $\mathcal{C}^{(4)}$ and the off-diagonal part of OTOC$^{(2)}$ ($\mathcal{C}^{(4)}_{\text{off-diag}}$, see 'Large-loop interference in OTOC$^{(2)}$' for a definition) decay algebraically and remain over 0.01 beyond $t = 20$. The standard deviation of a TOC, which does not have the echo-like structure of OTOCs, decays exponentially over time and becomes less than 0.01 at $t = 9$. The stark contrast between TOC and OTOCs indicates that the interferometric nature of the latter is crucial for enhancing sensitivities to quantum dynamics. In Supplementary Information section IV, we provide further studies of OTOC$^{(k)}$ fluctuations using one-dimensional Haar random circuits, finding that these observables decay as a power law consistent with the two-dimensional experimental data.

Large-loop interference in OTOC$^{(2)}$

The experiments performed in the preceding section, which change all details of U between OTOC measurements, is analogous to shifting the arms of an interferometer entirely (Fig. 1b). In this section, we demonstrate that higher-order OTOCs also become increasingly more sensitive to the phases of the interferometer arms, a hallmark of interference phenomena. Conceptually, many-body interference may be understood by first noting that equation (1) can, in the ergodic limit, be expressed as:

$$\mathcal{C}^{(2k)} = \text{Tr}\,[(B(t)M)^{(2k)}]/2^N. \quad (2)$$

For a given circuit instance, $B(t)$ can be decomposed in the basis of the 4^N Pauli strings $\{P_n\}$ of our N-qubit system:

$$B(t) = \sum_{n=1}^{4^N} b_n(t) P_n, \quad (3)$$

where $\{b_n\}$ is a set of real-valued time-dependent coefficients. The time evolution of B is visualized in the bottom left panel of Fig. 3a, where B is seen to branch out in Pauli space over time due to the action of non-Clifford gates in our circuits, creating the so-called operator entanglement[18,29,30]. In the schematic, the trajectories of some Pauli strings (shaded areas) are also seen to recombine during the time evolution. This mechanism, which affects both $\mathcal{C}^{(4)}$ and $\mathcal{C}^{(2)}$, will be referred to as small-loop interference.

The mechanism of large-loop interference is related to how Pauli strings at the end of the time evolution contribute to the experimental observable. It is present only in $\mathcal{C}^{(4)}$, as schematically shown in the upper panels of Fig. 3a. As $MP_nM = \pm P_n$, equation (2) can be written for $\mathcal{C}^{(4)}$ as:

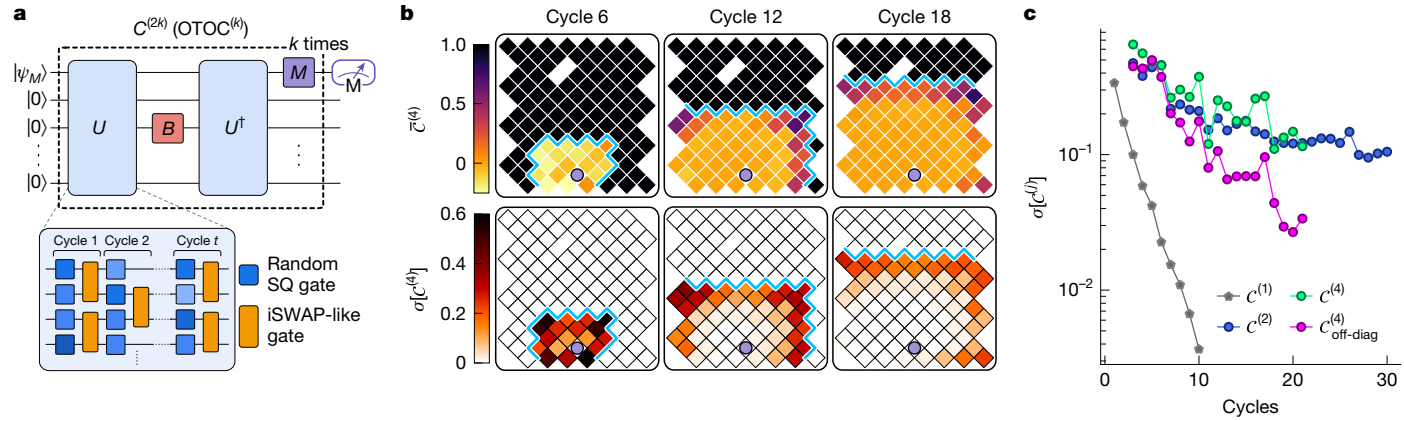

Fig. 2 | Sensitivity of OTOCs towards microscopic details of quantum dynamics. a, Top, quantum circuit schematic for measuring OTOCs of different orders, OTOC$^{(k)}$. Here, $|\psi_M\rangle$ is an eigenstate of the measurement operator M (realized as Z in this work). The operator B is realized as X. Bottom, implementation of the unitary U as t cycles of single- and two-qubit gates. Each single-qubit gate is $\exp\left(-i\frac{\theta}{2}(\cos(\phi)X+\sin(\phi)Y)\right)$, where $\theta/\pi \in \{0.25, 0.5, 0.75\}$ and ϕ/π is chosen randomly from the interval $[-1, 1]$. Each iSWAP-like gate is equivalent to an iSWAP followed by a CPHASE gate with a conditional phase of approximately 0.35 rad. **b**, The mean ($\bar{C}^{(4)}$) and standard deviation ($\sigma[C^{(4)}]$) of OTOC$^{(2)}$ ($C^{(4)}$) measured over 100 circuit instances for $t = 6, 12$ and 18 cycles. The colour at each qubit site indicates data collected with B applied to the given qubit. Purple dots indicate the fixed location of q_m. Cyan lines represent the light cone of q_m. **c**, Standard deviation of four quantities, TOC ($C^{(1)}$), OTOC ($C^{(2)}$), OTOC$^{(2)}$ ($C^{(4)}$) and the off-diagonal component of OTOC$^{(2)}$ ($C^{(4)}_{\text{off-diag}}$). For $C^{(2)}$, $C^{(4)}$ and $C^{(4)}_{\text{off-diag}}$, q_m has the same fixed location as in **b** whereas q_b gradually moves further from q_m as the number of circuit cycles increases, such that the OTOC mean $\bar{C}^{(2)} \approx 0.5$ is maintained. $C^{(1)}$ corresponds to $\langle Z(t)Z\rangle$ measured at a qubit close to the centre of the lattice. SQ, single qubit.

$$C^{(4)} = \sum_{\alpha,\beta,\gamma,\delta} c_{\alpha\beta\gamma\delta}\ \mathrm{Tr}\left[P_\alpha P_\beta P_\gamma P_\delta\right]. \tag{4}$$

Here each $c_{\alpha\beta\gamma\delta}$ is also a real-valued coefficient. Each Pauli string in this expression is represented as a coloured segment in the diagrams within the top panels of Fig. 3a. The length of this segment qualitatively represents the Hamming distance between the Pauli string and the identity. Multiplying two Pauli strings joins them at one end and forms a new Pauli string connecting the two new terminal points.

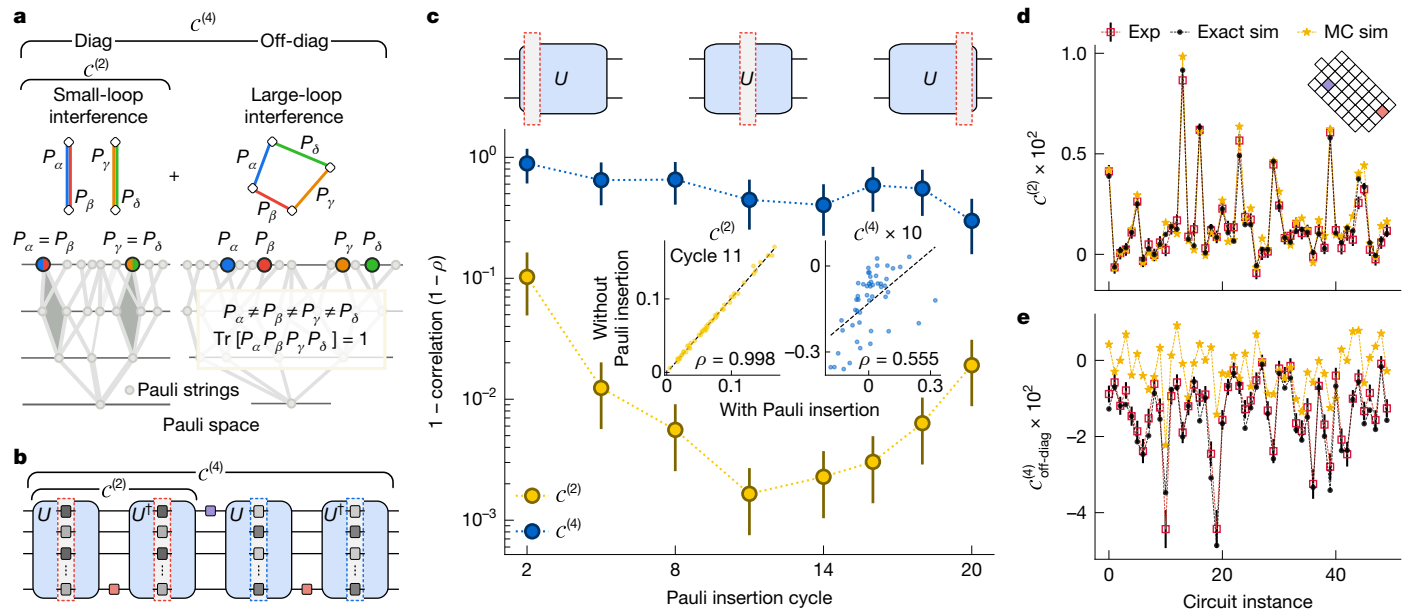

Fig. 3 | Quantum interference and classical simulation complexity of OTOC$^{(2)}$. a, In the Heisenberg picture, the time-evolved $B(t)$ branches into a superposition of multi-qubit Pauli strings. For $C^{(2)}$, in which only two copies of $B(t)$ are present, the final strings P_α and P_β need to be identical to contribute. For $C^{(4)}$, the strings $(P_\alpha, P_\beta, P_\gamma, P_\delta)$ contribute a 'diagonal' component $C^{(4)}_{\text{diag}}$ when $P_\alpha = P_\beta$ and $P_\gamma = P_\delta$, or an 'off-diagonal' component $C^{(4)}_{\text{off-diag}}$ when $P_\alpha \neq P_\beta \neq P_\gamma \neq P_\delta$. **b**, Protocol for probing quantum interference. Random Pauli operators are inserted at one circuit cycle, which changes the signs of the Pauli string coefficients. **c**, Relative signal change, characterized by $1-\rho$, as a function of the cycle at which Paulis are inserted. ρ refers to the Pearson correlation between experimental data from 50 different 40-qubit circuits ($t = 22$ cycles), obtained with and without Pauli insertion. Error bars denote standard errors estimated from resampling the experimental data. Insets, Data at cycle 11. **d**, Comparison of experimental $C^{(2)}$ values against exactly simulated $C^{(2)}$ for a set of 40-qubit circuit instances. Values computed using CMC heuristic algorithms are shown for comparison, achieving an SNR of 5.3, like that of the quantum processor (SNR = 5.4). Inset, circuit geometry (red for q_m and blue for q_b) used for the experiments in **c**–**e**. **e**, Experimental $C^{(4)}_{\text{off-diag}}$ values on the same set of 40 qubits, alongside exact and CMC simulations. $C^{(4)}_{\text{off-diag}}$ is measured by subtracting the Pauli-averaged $C^{(4)}$ from the non-averaged $C^{(4)}$. Here the experimental SNR is 3.9 whereas the SNR from CMC is 1.1. Error bars on experimental data are based on an empirical error model discussed in Supplementary Information sections II.F.3 and II.F.4. Exp, experiment; MC, Monte Carlo; sim, simulation.

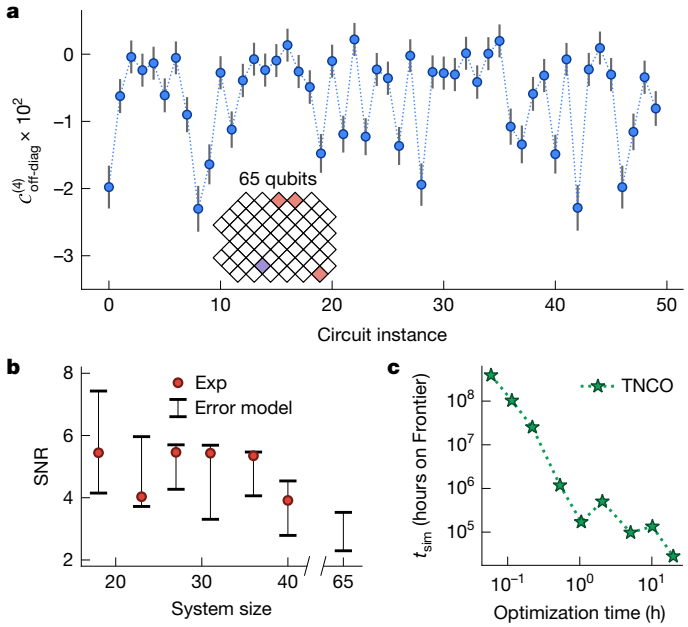

Fig. 4 | Measuring OTOC$^{(2)}$ in the classically challenging regime. a, $\mathcal{C}^{(4)}_{\text{off-diag}}$ measured on a set of 65-qubit circuits each having $t = 23$ cycles. Inset, Qubit geometry. B acts simultaneously on three different qubits. **b**, Experimental SNRs for circuits measured with system sizes ranging from 18 to 40 qubits. Error bars correspond to the 95% confidence interval of an empirical error model (Supplementary Information sections II.F.3 and II.F.4). Error bars in **a** are based on the same empirical error model. **c**, Estimated time to compute $\mathcal{C}^{(4)}_{\text{off-diag}}$ of a single circuit in **a** on the Frontier supercomputer using tensor-network contraction. The estimate was obtained by running a specially designed optimization algorithm[46–49] on 20 Google Cloud virtual machines (totalling 1,200 CPUs) up to a period of 24 h (x axis). Estimates using a publicly available library cotengra[47] lead to costs that are ten times higher after the same optimization time. TNCO, tensor-network contraction.

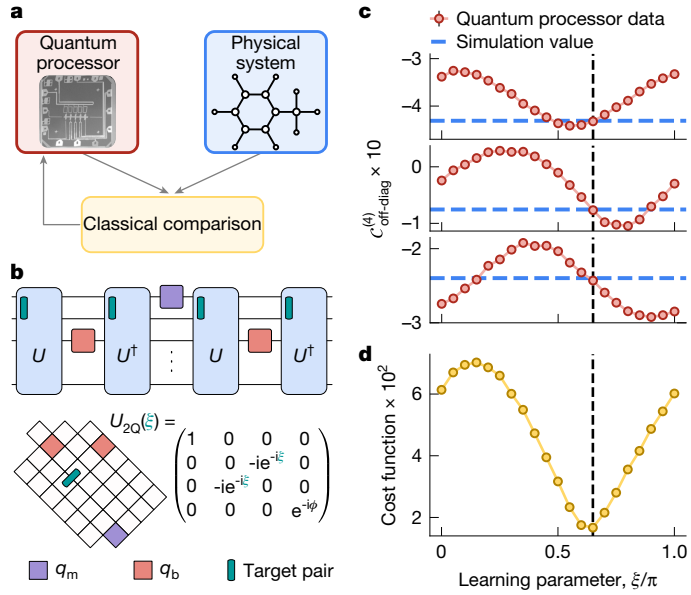

Fig. 5 | Application to Hamiltonian learning. a, Scheme for applying OTOC$^{(2)}$ in Hamiltonian learning. OTOC$^{(2)}$ measured in a physical system of interest is compared with a quantum simulation of OTOC$^{(2)}$ using a parameterized Hamiltonian of the same system. Hamiltonian parameters are then optimized to minimize the difference between the two datasets. **b**, Demonstrating a one-parameter learning experiment. A collection of classically simulated $\mathcal{C}^{(4)}_{\text{off-diag}}$ values from 20 circuit instances having a 34-qubit geometry (bottom left panel) are treated as data from a physical system of interest. The goal is to learn a particular phase $\xi/\pi = 0.6$ of the two-qubit gate unitary U_{2Q} belonging to one pair of qubits (green bar in the top and bottom left panels). **c**, Experimentally measured $\mathcal{C}^{(4)}_{\text{off-diag}}$ (quantum processor data) as a function of ξ for three different circuit instances. Blue lines indicate the ideal values of $\mathcal{C}^{(4)}_{\text{off-diag}}$ from a classical simulation. These lines intersect all three datasets close to the target value of ξ (vertical dashed line). **d**, An optimization cost function, corresponding to the root-mean-square difference between the quantum processor data and the classical simulation data of all 20 circuit instances as a function of ξ. The cost function is minimized at the target value of ξ.

For the trace in equation (4) to be non-zero, the product of the four Pauli strings must be the identity, that is, the diagram must form a loop. This condition is satisfied through two distinct means. If $\alpha = \beta$ and $\gamma = \delta$, we obtain the so-called diagonal contribution $\mathcal{C}^{(4)}_{\text{diag}}$ to $\mathcal{C}^{(4)}$ in which the loops enclose zero area. If $\alpha \neq \beta \neq \gamma \neq \delta$, we obtain the off-diagonal contribution $\mathcal{C}^{(4)}_{\text{off-diag}}$, named because each term may be thought of as an off-diagonal element in the $4^{4N} \times 4^{4N}$ density matrix formed by the Paulis. Diagrammatically, $\mathcal{C}^{(4)}_{\text{off-diag}}$ consists of a superposition of operator loops, each of which contains three unconstrained Pauli strings and, therefore, encloses an arbitrarily large area. For comparison, large-loop interference is absent in $\mathcal{C}^{(2)}$, as only Pauli strings with $\alpha = \beta$ contribute, like $\mathcal{C}^{(4)}_{\text{diag}}$.

To characterize the effects of quantum interference, we insert random Pauli operators at different cycles within each application of U and $U^\dagger$ (Fig. 3b). The inserted Paulis randomize the signs of the coefficients $c_{\alpha\beta\gamma\delta}$ in equation (4) without changing their amplitudes. This is analogous to shifting the phase around an ordinary interference loop without changing its intensity. By ensemble-averaging over random Paulis and probing the changes in $\mathcal{C}^{(4)}$ or $\mathcal{C}^{(2)}$, the contribution of quantum interference to each observable can then be quantified. Figure 3c shows the experimentally measured $1 - \rho$, where ρ is the Pearson correlation between circuits with and without inserted Paulis. The inserted Paulis produce substantial changes in $\mathcal{C}^{(4)}$, indicating that the large-loop interference effects ($\mathcal{C}^{(4)}_{\text{off-diag}}$) are a dominant contribution to $\mathcal{C}^{(4)}$. By contrast, the signal change for $\mathcal{C}^{(2)}$ is much weaker overall, owing to the presence of only small-loop interference. The larger residual effect of Pauli insertion near the edges of U is attributed to the fact that quantum gates closer to the B and M operators have more weight in the resulting signals. We also note that $1 - \rho$ is slightly reduced at later insertion cycles for $\mathcal{C}^{(4)}$, which may arise from external decoherence processes that tend to reduce the visibility of quantum interference. Last, by subtracting the $\mathcal{C}^{(4)}$ of each circuit after Pauli insertion from its original value, the off-diagonal contribution $\mathcal{C}^{(4)}_{\text{off-diag}}$ can be experimentally extracted.

We find that the observed interference effects in $\mathcal{C}^{(2)}$ and $\mathcal{C}^{(4)}$ are closely connected to their complexities with respect to approximate classical simulation algorithms, as the degree of quantum interference sets the level of allowed classical approximation. For OTOC, we find that it is sometimes approximated well by combining exact wavefunction evolution with a Monte Carlo simulation that ignores the effects of small interference loops. Two such algorithms, cached Monte Carlo (CMC) and tensor networks Monte Carlo, are described in Supplementary Information section III.B. Figure 3d shows experimental $\mathcal{C}^{(2)}$ values from a set of circuits comprising 40 qubits, along with values of $\mathcal{C}^{(2)}$ computed using CMC. To quantify the accuracy of each dataset, we define a signal-to-noise ratio (SNR; Methods) against exactly simulated $\mathcal{C}^{(2)}$ values shown in the same figure. The SNR achieved by CMC (5.3) is close to the experimental SNR of 5.4. For the off-diagonal OTOC$^{(2)}$ ($\mathcal{C}^{(4)}_{\text{off-diag}}$), classical algorithms are far less accurate and achieve a much lower SNR (1.1) compared with the experiment (3.9), as shown in Fig. 3e. In Supplementary Information section III.C, we review all classical simulation algorithms attempted as part of this work and show that none succeeds in approximating $\mathcal{C}^{(4)}_{\text{off-diag}}$.

Towards practical quantum advantage

The combination of large sensitivity and high classical simulation complexity makes higher-order OTOCs such as OTOC$^{(2)}$ a prime candidate for achieving the long-standing goal of practical quantum advantage. To illustrate this potential, we perform two more experiments, which show: (1) OTOC$^{(2)}$ can be accurately resolved in regimes that are, at present, intractable with classical supercomputers. (2) A specific example wherein OTOC$^{(2)}$ is used to accomplish a practical task.

We begin by demonstrating (1). Figure 4a shows a set of $\mathcal{C}^{(4)}_{\text{off-diag}}$ measurements performed with a 65-qubit geometry with B applied simultaneously to three different qubits, chosen to maximize the effective quantum volume (corresponding to the number of two-qubit gates falling within the light cones of the B and M operators[31]). To estimate the accuracy of these measurements, we next characterize the experimental error (SNR) across six different system sizes of up to 40 qubits (Fig. 4b). Here we observe that the SNR degrades only weakly as the system size increases and is also captured by the confidence interval of an empirical error model detailed in Supplementary Information sections II.F.3 and II.F.4. Based on the same error model, the SNR of the 65-qubit dataset is projected to range from 2 to 3. Given that classical heuristic algorithms are unable to achieve this accuracy (Supplementary Information section III.C), tensor-network contraction is the most effective approach toward classically simulating the same circuits. Figure 4c shows the estimated cost of simulating $\mathcal{C}^{(4)}_{\text{diag}}$ through tensor-network contraction on the Frontier supercomputer, which converges to approximately 3.2 years. This is a factor of approximately 13,000 longer than the experimental data collection time of 2.1 h per circuit, indicating that this experiment is, at present, in the beyond-classical regime of quantum computation.

To apply OTOCs in real-world applications, we consider a physical system of interest characterized by a Hamiltonian with a set of unknown parameters. The physical system supplies a collection of OTOC$^{(2)}$ data, which is compared against a quantum simulation of the same Hamiltonian. The unknown parameters are then optimized until the quantum-simulated data match the real-world experimental data (Fig. 5a). The slowly decaying signal size and sensitivity of OTOC$^{(2)}$, as demonstrated in Figs. 2 and 3, make it a particularly suitable candidate for accomplishing this task, which is known as Hamiltonian learning[32–35].

To demonstrate the proposed scheme in practice, we construct a one-parameter learning example, as shown in Fig. 5b. A set of $\mathcal{C}^{(4)}_{\text{off-diag}}$ values from 20 random circuit instances, produced by a classical simulation to mimic the role of the 'physical system' in Fig. 5a, are provided. All details of U, except the phase ξ of one two-qubit gate located along the passage between q_m and q_b, are also given. To learn the unknown parameter ξ, we measure $\mathcal{C}^{(4)}_{\text{off-diag}}$ on the quantum processor while varying ξ. Results for three circuit instances are shown in Fig. 5c, where we see smooth oscillations of experimental signals that are distinct between different instances. Importantly, all oscillations intersect the classically simulated values of $\mathcal{C}^{(4)}_{\text{off-diag}}$ at the target value of ξ. This is further reflected in Fig. 5d, where we have constructed a cost function between the classically simulated and experimentally measured values of $\mathcal{C}^{(4)}_{\text{off-diag}}$. The cost function has a global minimum at the target ξ value.

Conclusion

In this work, we have shown that OTOCs have quantum interference effects that endow them with a high sensitivity to details of the quantum dynamics and, for OTOC$^{(2)}$, also high levels of classical simulation complexity. As such, OTOCs are viable candidates for realizing practical quantum advantage, a chief milestone sought by recent experiments[36–38]. Generally, practical quantum advantage can be formulated as the task of measuring the expectation values of low-rank observables, for example, energy or correlations[3,39], such that:

(1) The observable can be experimentally measured with the proper accuracy, in our case with an SNR above unity. More formally, the observable is in the bounded-error quantum polynomial-time (BQP) class[40].
(2) The observable lies beyond the reach of both exact classical simulation and heuristic methods that trade accuracy for efficiency[31,41–44].

Satisfying both defines a 'Goldilocks zone' for quantum advantage. To demonstrate practical quantum advantage, one more criterion is required:
(3) The observable should yield practically relevant information about the quantum system.

Here, by measuring a many-body observable with SNR > 2 and showing that it is beyond the reach of currently known classical simulation algorithms, we have made progress towards (1) and (2). Moreover, a proof-of-principle for (3) is demonstrated with a dynamic learning problem. Although the random circuits used in the dynamic learning demonstration remain a toy model for Hamiltonians that are of practical relevance, the scheme is readily applicable to real physical systems. One such example is solid-state nuclear magnetic resonance systems, where dipolar couplings between spin pairs can be inverted without complete knowledge of their strength[45]. Comparing experimental data from such systems with quantum simulation outcomes may allow more accurate estimates of these couplings. We leave this exciting real-world application for future work.

Online content

Any methods, additional references, Nature Portfolio reporting summaries, source data, extended data, supplementary information, acknowledgements, peer review information; details of author contributions and competing interests; and statements of data and code availability are available at https://doi.org/10.1038/s41586-025-09526-6.

1. Feynman, R. P. Simulating physics with computers. *Int. J. Theor. Phys.* **21**, 467–488 (1982).
2. Lloyd, S. Universal quantum simulators. *Science* **273**, 1073–1078 (1996).
3. Altman, E. et al. Quantum simulators: architectures and opportunities. *PRX Quantum* **2**, 017003 (2021).
4. Baum, J., Munowitz, M., Garroway, A. N. & Pines, A. Multiple–quantum dynamics in solid state NMR. *J. Chem. Phys.* **83**, 2015–2025 (1985).
5. Larkin, A. I. & Ovchinnikov, Y. N. Quasiclassical method in the theory of superconductivity. *Sov. Phys. JETP* **28**, 1200–1205 (1969).
6. Shenker, S. H. & Stanford, D. Black holes and the butterfly effect. *J. High Energy Phys.* **2014**, 67 (2014).
7. Hosur, P. et al. Chaos in quantum channels. *J. High Energy Phys.* **2016**, 4 (2016).
8. Maldacena, J., Shenker, S. H. & Stanford, D. A bound on chaos. *J. High Energy Phys.* **2016**, 106 (2016).
9. Swingle, B. et al. Measuring the scrambling of quantum information. *Phys. Rev. A* **94**, 040302 (2016).
10. Aleiner, I. et al. Microscopic model of quantum butterfly effect: out-of-time-order correlators and traveling combustion waves. *Ann. Phys.* **375**, 378–406 (2016).
11. Roberts, D. & Yoshida, B. Chaos and complexity by design. *J. High Energy Phys.* **2017**, 121 (2017).
12. Gärttner, M. et al. Measuring out-of-time-order correlations and multiple quantum spectra in a trapped-ion quantum magnet. *Nat. Phys.* **13**, 781–786 (2017).
13. Nahum, A., Vijay, S. & Haah, J. Operator spreading in random unitary circuits. *Phys. Rev. X* **8**, 021014 (2018).
14. von Keyserlingk, C. W. et al. Operator hydrodynamics, OTOCs, and entanglement growth in systems without conservation laws. *Phys. Rev. X* **8**, 021013 (2018).
15. Rakovszky, T. et al. Diffusive hydrodynamics of out-of-time-ordered correlators with charge conservation. *Phys. Rev. X* **8**, 031058 (2018).
16. Khemani, V. et al. Operator spreading and the emergence of dissipative hydrodynamics under unitary evolution with conservation laws. *Phys. Rev. X* **8**, 031057 (2018).
17. Landsman, K. et al. Verified quantum information scrambling. *Nature* **567**, 61–65 (2019).
18. Mi, X. et al. Information scrambling in quantum circuits. *Science* **374**, 1479–1483 (2021).
19. Davis, E. et al. Approaching the Heisenberg limit without single-particle detection. *Phys. Rev. Lett.* **116**, 053601 (2016).
20. Li, Z. et al. Improving metrology with quantum scrambling. *Science* **380**, 1381–1384 (2023).
21. Hayden, P. & Preskill, J. Black holes as mirrors: quantum information in random subsystems. *J. High Energy Phys.* **2007**, 120 (2007).
22. Sekino, Y. & Susskind, L. Fast scramblers. *J. High Energy Phys.* **2008**, 065 (2008).
23. Xu, S. & Swingle, B. Locality, quantum fluctuations, and scrambling. *Phys. Rev. X* **9**, 031048 (2019).

24. Kaufman, A. M. et al. Quantum thermalization through entanglement in an isolated many-body system. *Science* **353**, 794–800 (2016).
25. Zhou, Z. et al. Thermalization dynamics of a gauge theory on a quantum simulator. *Science* **377**, 311–314 (2022).
26. Zhang, X. et al. A superconducting quantum simulator based on a photonic-bandgap metamaterial. *Science* **379**, 278–283 (2023).
27. Andersen, T. I. et al. Thermalization and criticality on an analogue–digital quantum simulator. *Nature* **638**, 79–85 (2025).
28. Braumüller, J. et al. Probing quantum information propagation with out-of-time-ordered correlators. *Nat. Phys.* **18**, 172–178 (2022).
29. Zanardi, P. Entanglement of quantum evolutions. *Phys. Rev. A* **63**, 040304 (2001).
30. Garcia, R. J., Bu, K. & Jaffe, A. Resource theory of quantum scrambling. *Proc. Natl Acad. Sci. USA* **120**, e2217031120 (2023).
31. Kechedzhi, K. et al. Effective quantum volume, fidelity and computational cost of noisy quantum processing experiments. *Future Gener. Comput. Syst.* **153**, 431–441 (2024).
32. Bairey, E. et al. Learning a local Hamiltonian from local measurements. *Phys. Rev. Lett.* **122**, 020504 (2019).
33. O'Brien, T. E. et al. Quantum computation of molecular structure using data from challenging-to-classically-simulate nuclear magnetic resonance experiments. *PRX Quantum* **3**, 030345 (2022).
34. Cotler, J., Schuster, T. & Mohseni, M. Information-theoretic hardness of out-of-time-order correlators. *Phys. Rev. A* **108**, 062608 (2023).
35. Schuster, T. et al. Learning quantum systems via out-of-time-order correlators. *Phys. Rev. Res.* **5**, 043284 (2023).
36. Kim, Y. et al. Evidence for the utility of quantum computing before fault tolerance. *Nature* **618**, 500–505 (2023).
37. King, A. D. et al. Beyond-classical computation in quantum simulation. *Science* **388**, 199–204 (2025).
38. Haghshenas, R. et al. Digital quantum magnetism at the frontier of classical simulations. Preprint at https://arxiv.org/abs/2503.20870 (2025).
39. Daley, A. J. et al. Practical quantum advantage in quantum simulation. *Nature* **607**, 667–676 (2022).
40. Bernstein, E. & Vazirani, U. Quantum complexity theory. *SIAM J. Comput.* **26**, 1411–1473 (1997).
41. Tindall, J., Fishman, M., Stoudenmire, E. M. & Sels, D. Efficient tensor network simulation of IBM's Eagle kicked Ising experiment. *PRX Quantum* **5**, 010308 (2024).
42. Begušić, T. et al. Fast and converged classical simulations of evidence for the utility of quantum computing before fault tolerance. *Sci. Adv.* **10**, eadk4321 (2024).
43. Tindall, J. et al. Dynamics of disordered quantum systems with two- and three-dimensional tensor networks. https://arxiv.org/abs/2503.05693 (2025).
44. Mauron, L. & Carleo, G. Challenging the quantum advantage frontier with large-scale classical simulations of annealing dynamics. https://arxiv.org/abs/2503.08247 (2025).
45. Rhim, W.-K. et al. Time-reversal experiments in dipolar-coupled spin systems. *Phys. Rev. B* **3**, 684–696 (1971).
46. Boixo, S. et al. Simulation of low-depth quantum circuits as complex undirected graphical models. https://arxiv.org/abs/1712.05384 (2017).
47. Gray, J. & Kourtis, S. Hyper-optimized tensor network contraction. *Quantum* **5**, 410 (2021).
48. Kalachev, G. et al. Multi-tensor contraction for XEB verification of quantum circuits. https://arxiv.org/abs/2108.05665 (2022).
49. Pan, F., Chen, K. & Zhang, P. Solving the sampling problem of the Sycamore quantum circuits. *Phys. Rev. Lett.* **129**, 090502 (2022).

Google Quantum AI and Collaborators

Dmitry A. Abanin[1,2], Rajeev Acharya[1], Laleh Aghababaie-Beni[1], Georg Aigeldinger[1], Ashok Ajoy[3,4,5], Ross Alcaraz[1], Igor Aleiner[1], Trond I. Andersen[1], Markus Ansmann[1], Frank Arute[1], Kunal Arya[1], Abraham Asfaw[1], Nikita Astrakhantsev[1], Juan Atalaya[1], Ryan Babbush[1], Dave Bacon[1], Brian Ballard[1], Joseph C. Bardin[1,6], Christian Bengs[3,4], Andreas Bengtsson[1], Alexander Bilmes[1], Sergio Boixo[1], Gina Bortoli[1], Alexandre Bourassa[1], Jenna Bovaird[1], Dylan Bowers[1], Leon Brill[1], Michael Broughton[1], David A. Browne[1], Brett Buchea[1], Bob B. Buckley[1], David A. Buell[1], Tim Burger[1], Brian Burkett[1], Nicholas Bushnell[1], Anthony Cabrera[1], Juan Campero[1], Hung-Shen Chang[1], Yu Chen[1], Zijun Chen[1], Ben Chiaro[1], Liang-Ying Chih[1], Desmond Chik[1], Charina Chou[1], Jahan Claes[1], Agnetta Y. Cleland[1], Josh Cogan[1], Saul Cohen[7], Roberto Collins[1], Paul Conner[1], William Courtney[1], Alexander L. Crook[1], Ben Curtin[1], Sayan Das[1], Laura De Lorenzo[1], Dripto M. Debroy[1], Sean Demura[1], Michel Devoret[1,8], Agustin Di Paolo[1], Paul Donohoe[1], Ilya Drozdov[1,9], Andrew Dunsworth[1], Clint Earle[1], Alec Eickbusch[1], Aviv Moshe Elbag[1], Mahmoud Elzouka[1], Catherine Erickson[1], Lara Faoro[1], Edward Farhi[1], Vinicius S. Ferreira[1], Leslie Flores Burgos[1], Ebrahim Forati[1], Austin G. Fowler[1], Brooks Foxen[1], Suhas Ganjam[1], Gonzalo Garcia[1], Robert Gasca[1], Élie Genois[1], William Giang[1], Craig Gidney[1], Dar Gilboa[1], Raja Gosula[1], Alejandro Grajales Dau[1], Dietrich Graumann[1], Alex Greene[1], Jonathan A. Gross[1], Hanfeng Gu[7], Steve Habegger[1], John Hall[1], Ikko Hamamura[7], Michael C. Hamilton[1,10], Monica Hansen[1], Matthew P. Harrigan[1], Sean D. Harrington[1], Stephen Heslin[1], Paula Heu[1], Oscar Higgott[1], Gordon Hill[1], Jeremy Hilton[1], Sabrina Hong[1], Hsin-Yuan Huang[1], Ashley Huff[1], William J. Huggins[1], Lev B. Ioffe[1], Sergei V. Isakov[1], Justin Iveland[1], Evan Jeffrey[1], Zhang Jiang[1], Xiaoxuan Jin[1], Cody Jones[1], Stephen Jordan[1], Chaitali Joshi[1], Pavol Juhas[1], Andreas Kabel[1], Dvir Kafri[1], Hui Kang[1], Amir H. Karamlou[1], Kostyantyn Kechedzhi[1], Julian Kelly[1], Trupti Khaire[1], Tanuj Khattar[1], Mostafa Khezri[1], Seon Kim[1], Robbie King[1,11,12], Paul V. Klimov[1], Andrey R. Klots[1], Bryce Kobrin[1], Alexander N. Korotkov[1], Fedor Kostritsa[1], Robin Kothari[1], John Mark Kreikebaum[1], Vladislav D. Kurilovich[1], Elica Kyoseva[7], David Landhuis[1], Tiano Lange-Dei[1], Brandon W. Langley[1], Pavel Laptev[1], Kim-Ming Lau[1], Loïck Le Guevel[1], Justin Ledford[1], Joonho Lee[1,13], Kenny Lee[1], Yuri D. Lensky[1], Shannon Leon[1], Brian J. Lester[1], Wing Yan Li[1], Alexander T. Lill[1], Wayne Liu[1], William P. Livingston[1], Aditya Locharla[1], Erik Lucero[1], Daniel Lundahl[1], Aaron Lunt[1], Sid Madhuk[1], Fionn D. Malone[1], Ashley Maloney[1], Salvatore Mandrà[1,14,15], James M. Manyika[1], Leigh S. Martin[1], Orion Martin[1], Steven Martin[1], Yossi Matias[1], Cameron Maxfield[1], Jarrod R. McClean[1], Matt McEwen[1], Seneca Meeks[1], Anthony Megrant[1], Xiao Mi[1], Kevin C. Miao[1], Amanda Mieszala[1], Zlatko Minev[1], Reza Molavi[1], Sebastian Molina[1], Shirin Montazeri[1], Alexis Morvan[1], Ramis Movassagh[1], Wojciech Mruczkiewicz[1], Ofer Naaman[1], Matthew Neeley[1], Charles Neill[1], Ani Nersisyan[1], Hartmut Neven[1]✉, Michael Newman[1], Jiun How Ng[1], Anthony Nguyen[1], Murray Nguyen[1], Chia-Hung Ni[1], Murphy Yuezhen Niu[1,16], Logan Oas[1], Thomas E. O'Brien[1], William D. Oliver[1,17,18,19], Alex Opremcak[1], Kristoffer Ottosson[1], Andre Petukhov[1], Alex Pizzuto[1], John Platt[1], Rebecca Potter[1], Orion Pritchard[1], Leonid P. Pryadko[1,20], Chris Quintana[1], Ganesh Ramachandran[1], Chandrasekhar Ramanathan[21], Matthew J. Reagor[1], John Redding[1], David M. Rhodes[1], Gabrielle Roberts[1], Eliott Rosenberg[1], Emma Rosenfeld[1], Pedram Roushan[1], Nicholas C. Rubin[1], Negar Saei[1], Daniel Sank[1], Kannan Sankaragomathi[1], Kevin J. Satzinger[1], Alexander Schmidhuber[1], Henry F. Schurkus[1], Christopher Schuster[1], Thomas Schuster[11,22], Michael J. Shearn[1], Aaron Shorter[1], Noah Shutty[1], Vladimir Shvarts[1], Volodymyr Sivak[1], Jindra Skruzny[1], Spencer Small[1], Vadim Smelyanskiy[1], W. Clarke Smith[1], Rolando D. Somma[1], Sofia Springer[1], George Sterling[1], Doug Strain[1], Jordan Suchard[1], Philippe Suchsland[1,23], Aaron Szasz[1], Alex Sztein[1], Douglas Thor[1], Eifu Tomita[1], Alfredo Torres[1], M. Mert Torunbalci[1], Abeer Vaishnav[1], Justin Vargas[1], Sergey Vdovichev[1], Guifre Vidal[1], Benjamin Villalonga[1], Catherine Vollgraff Heidweiller[1], Steven Waltman[1], Shannon X. Wang[1], Brayden Ware[1], Kate Weber[1], Travis Weidel[1], Tom Westerhout[1], Theodore White[1], Kristi Wong[1], Bryan W. K. Woo[1], Cheng Xing[1], Z. Jamie Yao[1], Ping Yeh[1], Bicheng Ying[1], Juhwan Yoo[1], Noureldin Yosri[1], Grayson Young[1], Adam Zalcman[1], Chongwei Zhang[3], Yaxing Zhang[1], Ningfeng Zhu[1] & Nicholas Zobrist[1]

[1]Google Research, Mountain View, CA, USA. [2]Department of Physics, Princeton University, Princeton, NJ, USA. [3]Department of Chemistry, University of California Berkeley, Berkeley, CA, USA. [4]Chemical Sciences Division, Lawrence Berkeley National Laboratory, Berkeley, CA, USA. [5]CIFAR Azrieli Global Scholars Program, CIFAR, Toronto, Ontario, Canada. [6]Department of Electrical and Computer Engineering, University of Massachusetts, Amherst, MA, USA. [7]NVIDIA Corporation, Santa Clara, CA, USA. [8]Department of Physics, University of California, Santa Barbara, CA, USA. [9]Department of Physics, University of Connecticut, Storrs, CT, USA. [10]Department of Electrical and Computer Engineering, Auburn University, Auburn, AL, USA. [11]Institute for Quantum Information and Matter, Caltech, Pasadena, CA, USA. [12]Computational and Mathematical Sciences, Caltech, Pasadena, CA, USA. [13]Department of Chemistry, Harvard University, Cambridge, MA, USA. [14]Quantum Artificial Intelligence Laboratory, NASA Ames Research Center, Moffett Field, CA, USA. [15]KBR, Houston, TX, USA. [16]Department of Computer Science, University of California, Santa Barbara, CA, USA. [17]Research Laboratory of Electronics, Massachusetts Institute of Technology, Cambridge, MA, USA. [18]Department of Electrical Engineering and Computer Science, Massachusetts Institute of Technology, Cambridge, MA, USA. [19]Department of Physics, Massachusetts Institute of Technology, Cambridge, MA, USA. [20]Department of Physics and Astronomy, University of California, Riverside, CA, USA. [21]Department of Physics and Astronomy, Dartmouth College, Hanover, NH, USA. [22]Walter Burke Institute for Theoretical Physics, Caltech, Pasadena, CA, USA. [23]Max Planck Institute for the Physics of Complex Systems, Dresden, Germany. ✉e-mail: neven@google.com

Methods

Quantum processor and random circuit sampling benchmark

The quantum processor originally comprised 105 frequency-tunable superconducting transmon qubits connected by tunable couplers. On cooling down, we found that two qubits were inoperable due to broken coupler bias lines. They were, therefore, excluded from the experiment. Details of the processor, including gate and read-out errors, qubit coherence times, anharmonicities and frequencies, can be found in Supplementary Information section II.A. Owing to improved single-qubit relaxation times T_1 (median of 106 μs) compared with our earlier quantum processors, a median two-qubit gate (iSWAP-like) error of 0.15% was achieved for this device. As a system-wide benchmark, we performed a random circuit sampling experiment and estimated the overall fidelity to be 0.001 at 40 circuit cycles, which doubles the circuit volume compared with previous records and corresponds to approximately 10^{25} years of simulation run-time on the Frontier supercomputer using tensor-network contraction algorithms (Supplementary Information section II.B).

Signal-to-noise ratio

The SNR is defined as follows. For the set of circuit-specific $\mathcal{C}^{(2)}$ (or $\mathcal{C}^{(4)}_{\text{off-diag}}$) values, the mean is subtracted, and they are then rescaled by their variance, $\mathcal{C}^{(s)} = (\mathcal{C} - \overline{\mathcal{C}})/\sigma(\mathcal{C})$ where $\mathcal{C}$ represents either $\mathcal{C}^{(2)}$ or $\mathcal{C}^{(4)}_{\text{off-diag}}$. This is done to both the set of experimentally measured ($\{\mathcal{C}_{\text{exp}}\}$) and the set of numerically simulated quantities ($\{\mathcal{C}_{\text{sim}}\}$). The SNR is then $1/\sqrt{\overline{(\mathcal{C}^{(s)}_{\text{exp}} - \mathcal{C}^{(s)}_{\text{sim}})^2}}$, where the overline denotes averaging over all circuit instances. This definition of SNR is directly related to the Pearson correlation coefficient ρ as $\text{SNR} = 1/\sqrt{2(1-\rho)}$.

Initial states

For measurements of $\mathcal{C}^{(2k)}$ with respect to a single initial state, an auxiliary qubit may be entangled with q_{m} after preparing the system in the desired initial state and then read out at the end. In our present work, we simplify this scheme by initializing q_{m} in the $|0\rangle$ state, which is an eigenstate of the measurement operator $M = Z$. Measuring q_{m} in the Z basis directly yields $\mathcal{C}^{(2k)}$.

It is also possible to measure $\mathcal{C}^{(2k)}$ of an infinite-temperature initial state, that is a maximally mixed state with the density matrix $I/2^N$, where I is the identity matrix and N is the number of qubits. This is done by averaging over different initial states. In Supplementary Information section II.E.4, we show measurements of infinite-temperature $\mathcal{C}^{(2)}$ after averaging over initial states in a set of 66-qubit circuits. A sizeable circuit-to-circuit fluctuation is still found in this case, indicating that the signal size of $\mathcal{C}^{(2k)}$ remains large even for infinite-temperature states.

Choice of circuit geometries

The various circuit geometries studied throughout this work were chosen with the following considerations: (1) For each system size, we placed q_{b} and q_{m} close to the opposing edges of a lattice. (2) The total number of circuit cycles for each system size was adjusted to be the maximum beyond which the average signal size for $\mathcal{C}^{(4)}_{\text{off-diag}}$ was reduced below 0.01. These two considerations were implemented such that each small-scale geometry (for example, the six different geometries used in Fig. 4c) mimic the geometry and overall signal size of the 65-qubit circuits in Fig. 4a.

Classical simulation costs of 40-qubit circuits

Each 40-qubit circuit instance in Fig. 3d,e required 3 h to simulate exactly on a Google Cloud virtual machine with 11.5 Tb of RAM and 416 CPUs. Matching the accuracy (SNR ≈ 5) of the quantum experiment in Fig. 3d using a CMC simulation required a cache size of 1 billion (see Supplementary Information section III.B.2 for a definition) and 6 days of simulation time (per circuit) on a single NVIDIA H100 GPU to gather sufficient statistics.

Circuit-to-circuit fluctuations of $\mathcal{C}^{(2k)}$

In Supplementary Information section IV we analyse the moments of $\mathcal{C}^{(2)}$ and $\mathcal{C}^{(4)}$ theoretically and numerically for the one-dimensional bricklayer circuit of two-qubit Haar random gates. For $\mathcal{C}^{(2)}$, we used a combination of perturbation theory and large-scale matrix product state simulations to relate the power-law circuit-to-circuit fluctuations to the small interference loops introduced in the main text. For $\mathcal{C}^{(4)}$ and $\mathcal{C}^{(4)}_{\text{off-diag}}$, a similar analysis is challenging and, instead, we verified the polynomial scaling of fluctuations with exact numerics. We also demonstrate the existence of a dynamical quantum phase transition in the spectrum of the operator $MB(t)$ (equation (2)). The properties of this transition were captured in an analytically tractable random matrix model, which allowed us to compute moments $k \geq 1$. This quantum criticality is consistent with the classically intractable power-law correlations in $\mathcal{C}^{(2k)}$.

Sign problem in computing $\mathcal{C}^{(4)}$

In 'Large-loop interference in OTOC$^{(2)}$', we demonstrated a significant independent contribution in equation (4) from non-paired trajectories in the space of Pauli strings ($\mathcal{C}^{(4)}_{\text{off-diag}}$ in Fig. 3a), which have coefficients with random signs. In Supplementary Information section III.C.3, we further argue theoretically that this interference is not an artefact of the Pauli representation but is intrinsic to $\mathcal{C}^{(4)}$. We accomplished this for the circuit-averaged $\mathcal{C}^{(4)}$, which is strictly easier to compute classically. We used a mapping between the average $\mathcal{C}^{(4)}$ and a model of a magnet that has the structure of the symmetric group of order 4, which reflects universal symmetries of the random circuit ensemble. We showed numerically that the sign problem in this model is severe. We, therefore, argue that the severe sign problem is an inevitable feature that presents a barrier for classical sampling algorithms when computing $\mathcal{C}^{(4)}$.

Data availability

The quantum circuits and data generated and analysed for this study are available at Zenodo (https://doi.org/10.5281/zenodo.15640502)[50].

Code availability

The source code used for the tensor contraction cost estimates are available under an open-source licence at GitHub (https://github.com/google-research/tnco).

50. Google Quantum AI. Circuits for the main text of 'Constructive interference at the edge of quantum ergodic dynamics'. *Zenodo* 10.5281/zenodo.15640502 (2025).

Acknowledgements We are grateful to A. Ashkenazi, S. Brin, S. Pichai and R. Porat for their executive sponsorship of the Google Quantum AI team and for their continued engagement and support.

Author contributions D.A.A., R. Acharya, L.A.-B., G.A., R. Alcaraz, I.A., T.I.A., M.A., F.A., K.A., A. Asfaw, N.A., J.A., R.B., D. Bacon, B. Ballard, J.C.B., A. Bengtsson, A. Bilmes, S.B., G.B., A. Bourassa, J.B., D. Bowers, L.B., M.B., D.A. Browne, B. Buchea, B.B.B., D.A. Buell, T.B., B. Burkett, N.B., A.C., J. Campero, H.-S.C., Y.C., Z.C., B. Chiaro, L.-Y.C., D.C., C.C., J. Cogan, A.Y.C., J. Claes, R.C., P.C., W.C., A.L.C., B. Curtin, S. Das, L.D.L., D.M.D., S. Demura, M.D., A.D.P., P.D., I.D., A.D., C. Earle, A.E., A.M.E., M.E., C. Erickson, L.F., E. Farhi, V.S.F., L.F.B., E. Forati, A.G.F., B.F., S.G., G.G., R. Gasca, É.G., W.G., C.G., D. Gilboa, R. Gosula, A.G.D., D. Graumann, A.G., J.A.G., S. Heslin, J. Hall, M.C.H., M.H., M.P.H., S.D.H., S. Habegger, P.H., O.H., G.H., J. Hilton, S. Hong, H.-Y.H., A.H., W.J.H., L.B.I., S.V.I., J.I., E.J., Z.J., X.J., C. Jones, S.J., C. Joshi, P.J., A.K., D.K., H.K., A.H.K., K.K., J.K., T. Khaire, T. Khattar, M.K., S.K., R. King, P.V.K., R. Kothari, B.K., A.N.K., F.K., R. Kothari, J.M.K., V.D.K., D. Landhuis, T.L.-D., B.W.L., P.L., K.-M.L., L.L.G., J. Ledford, J. Lee, K.L., Y.D.L., S.L., B.J.L., W.Y.L., A.T.L., W.L., W.P.L., A. Locharla, E.L., D. Lundahl, A. Lunt, S. Madhuk, F.D.M., A. Maloney, S. Mandrà, J.M.M., L.S.M., O.M., S. Molina, Y.M., C.M., J.R.M., M.M., S. Montazeri, A. Megrant, X.M., K.C.M., A. Mieszala, Z.M., R. Movassagh, S. Meeks, S. Martin, A. Morvan, R. Molavi, W.M., O.N., M. Neeley, C.N., A. Nersisyan, H.N., M. Newman, J.H.N., A. Nguyen, M. Nguyen, C.-H.N., M.Y.N., L.O., T.E.O., W.D.O., A.O., K.O., A. Petukhov, A. Pizzuto, J.P., R.P., O.P., L.P.P., C.Q., G. Ramachandran, M.J.R., J.R., D.M.R., G. Roberts, E. Rosenberg, E. Rosenfeld, P.R., N.C.R., N. Saei, D. Strain, K.S., K.J.S., A. Shorter, H.F.S., C.S., T.S., M.J.S., A. Szasz, N. Shutty, V. Shvarts, V. Sivak, J. Skruzny, S. Small, V. Smelyanskiy, W.C.S., R.D.S., S. Springer, G.S., D. Sank, J. Suchard, P.S., A. Sztein, A. Schmidhuber, D.T., E.T., A.T., M.M.T., A.V., J.V., S.V., G.V., B.V., C.V.H., S.W., S.X.W., B.W., K. Wong, T. Weidel, T. Westerhout, T. White, K. Weber, B.W.K.W., C.X., Z.J.Y., P.Y., B.Y., J.Y., N.Y., G.Y., A.Z., Y.Z., N. Zhu and N. Zobrist performed

the experiment, developed the theory behind the experiment, analysed the data and built the associated infrastructure supporting the experiment. S.C., H.G., I.H. and E.K. contributed to the classical simulation of OTOCs. A. Ajoy, C.Z., C.B. and C.R. contributed to the formulation of the Hamiltonian learning experiment. All authors participated in writing and revising the paper and Supplementary Information.

Competing interests The authors declare no competing interests.

Additional information

Supplementary information The online version contains supplementary material available at https://doi.org/10.1038/s41586-025-09526-6.

Correspondence and requests for materials should be addressed to Hartmut Neven.

Peer review information *Nature* thanks Morten Kjaergaard and the other, anonymous, reviewer(s) for their contribution to the peer review of this work. Peer reviewer reports are available.